Journal of *Marine Science and Engineering*

MDPI

Article

Modeling and Analysis of Actuators in Multi-Pump Waterjet Propulsion Systems

Shuli Jia [1], Yinuo Guo [2], Yuxue Liu [1], Dali Wei [2], Chong Qu [1] and Liyong Ma [2,*]

[1] Automation Engineering Department, Shanghai Marine Diesel Engine Research Institute, Shanghai 201108, China; shulijia@yeah.net (S.J.); liuyuxue_1977@sina.com (Y.L.); quchong@csic711.com (C.Q.)
[2] School of Information Science and Engineering, Harbin Institute of Technology, Weihai 264209, China; 2021210610@stu.hit.edu.cn (Y.G.); delaou@outlook.com (D.W.)
* Correspondence: maly@hitwh.edu.cn

Abstract: Waterjet propulsion, which generates thrust by ejecting water jets, has attracted significant attention in modern high-performance vessels due to its efficiency, superior cavitation resistance, and excellent maneuverability. While previous research has primarily concentrated on optimizing the overall performance of waterjet propulsion systems, insufficient attention has been paid to the detailed dynamic modeling of actuators in multi-pump systems, a critical component for improving system control precision. This paper addresses this gap by developing dynamic models for the reversing bucket and rudder angle actuators in marine waterjet propulsion systems. Based on an in-depth analysis of their working principles and operational parameters, transfer function models are established to simulate actuator performance under various conditions, including wear, hydraulic oil leakage, and external disturbances. Key influencing factors for each condition are identified, and corresponding parameter-setting models are constructed. The models' response speed and steady-state accuracy are validated through step and ramp tests, confirming their effectiveness and reliability. The proposed model is verified with real measurement experiments and comparisons. The findings of this study contribute new insights into the dynamic behavior of multi-pump waterjet propulsion systems and provide a solid theoretical foundation for the future development of optimized control strategies in complex marine propulsion environments.

Keywords: waterjet propulsion system; reversing bucket and rudder angle actuators; modeling

check for updates

Academic Editor: Alon Gany

Received: 8 October 2024
Revised: 9 January 2025
Accepted: 13 January 2025
Published: 17 January 2025

Citation: Jia, S.; Guo, Y.; Liu, Y.; Wei, D.; Qu, C.; Ma, L. Modeling and Analysis of Actuators in Multi-Pump Waterjet Propulsion Systems. *J. Mar. Sci. Eng.* **2025**, *13*, 154. https://doi.org/10.3390/jmse13010154

Copyright: © 2025 by the authors. Licensee MDPI, Basel, Switzerland. This article is an open access article distributed under the terms and conditions of the Creative Commons Attribution (CC BY) license (https://creativecommons.org/licenses/by/4.0/).

1. Introduction

Waterjet propulsion, known for its high efficiency, superior anti-cavitation capability, excellent maneuverability, simple transmission system, low noise, and wide operational range, has become increasingly popular in high-performance vessels such as small waterplane area twin-hull ships, hydrofoils, and wave-piercing catamarans [1,2]. Equipped with steering and reversing mechanisms, waterjet-propelled ships can flexibly adjust the waterjet direction based on propulsion control system commands, enabling complex maneuvers. Compared to traditional propeller propulsion systems, waterjet propulsion significantly enhances both cavitation resistance and propulsion efficiency [3].

In recent years, notable advances have been made in the dynamic modeling and numerical simulation of waterjet propulsion systems [4–8]. While most studies have focused on performance optimization and propulsion system modeling, some research has utilized computational fluid dynamics (CFD), often combined with physical model experiments, to analyze the hydrodynamic performance and internal/external flow field characteristics of

waterjet-propelled vessels [9,10]. For example, in the area of hydrodynamic performance analysis, studies have explored the characteristics of the air intake ducts of waterjet systems [11]. Through planar motion mechanism experiments, researchers have evaluated course-keeping capabilities at various ship speeds and obtained relevant hydrodynamic coefficients [12]. Building on this, Kandasamy et al. developed a simplified pump model by integrating CFD simulations with experimental data, validating the relationship between waterjet input variables [13]. Meanwhile, Gong et al. examined the steering and navigation mechanisms of waterjet systems, analyzing hydrodynamic performance and establishing models. They designed a load disturbance observer to improve control accuracy and system stability [14].

In recent years, research on hydrodynamic analysis has primarily focused on the CFD method, which can simulate the fluid flow conditions inside waterjet propulsors, including flow velocity, pressure distribution, vortex structures, and more. The simulation results provide insights into the characteristics of the flow field inside waterjet propulsors. Zhang, H., et al. [15] studied an independently developed low-wake underwater jet propulsion system as their research subject. They employed the CFD method, combining adaptive mesh refinement techniques with the volume of fluid (VOF) model to achieve high accuracy and capture a wide range of flow field information. Zhang, L., et al. [16] proposed four CFD-based numerical models for waterjet-propelled trimarans using overset grids, which directly simulate the real-time motion of ships in various complex environments. Guo, J., et al. [17] optimized the piping and nozzles in the system based on the CFD method, conducting parametric geometric reconstruction of the ducts and nozzles. Besides the CFD method, Gong, J., et al. [18] used the RANS method to study the inflow and thrust characteristics of waterjet propulsion under oblique flow conditions ranging from 0 to 30 degrees, proposing and validating an estimation formula for the waterjet's propulsion thrust under oblique flow conditions. Gong, J., et al. [19] also systematically analyzed the scale effects on several hydrodynamic coefficients and flow field details. Feng, R., et al. [20] conducted numerical simulations of the flow field characteristics of waterjet propulsion under mooring conditions based on mooring experiments using a VOF-based computational method to analyze the internal flow characteristics of waterjet propulsion under mooring conditions. Chen, T.-R., et al. [21] revealed the influence of inflow conditions on propulsion performance through numerical simulations of axial waterjet propellers at different inflow velocities and angles. Xu, S., et al. conducted in-depth research on the specific mechanisms of cavitation phenomena in jet pumps, employing the detached eddy simulation (DES) turbulence model and the Zwart–Gerber-Belamri (ZGB) cavitation model for simulations [22].

In the area of control algorithms for waterjet propulsion, Jiang et al. proposed a synchronous control strategy combined with a mirror equal-angle thrust control strategy, successfully implementing vector control for waterjet-propelled vessels [23]. Other studies have explored the application of sliding mode control, model predictive control (MPC), and neural network control. For example, Gong et al. developed a transfer function model for the waterjet steering system, designed a disturbance observer based on this model, and implemented a global sliding mode controller. Simulation results showed high accuracy, strong tracking performance, and robust control [24]. Notably, model predictive control has achieved significant success in process control, with model-based controllers outperforming traditional PID controllers in various applications [25,26]. In neural network control, researchers have examined strategies combining neural networks and PID control [27], as well as fuzzy model reference learning control for energy efficiency and disturbance rejection [28]. PID-based backpropagation (BP) neural network control strategies have also demonstrated strong adaptability and robustness [29]. Additionally,

Xu, Z., et al. proposed a sliding mode control strategy for marine diesel engines in waterjet-propelled ships based on affine nonlinear models [30].

Although existing research has laid a strong theoretical foundation for the design and optimization of waterjet propulsion systems, further investigation into multi-pump systems is necessary to achieve more efficient and reliable propulsion solutions. Specifically, control algorithms for multi-pump systems need to be refined to adapt to increasingly complex operational environments and to improve control precision. Additionally, there is a notable lack of detailed modeling studies on the actuators within multi-pump propulsion systems. This gap in the literature hinders a deeper understanding of the dynamic characteristics of these systems and limits the potential for achieving higher propulsion efficiency.

To address this gap, this study focuses on the dynamic modeling and simulation of actuators in multi-pump waterjet propulsion systems. The innovative aspects of this research include the development of transfer function models for the reversing bucket and rudder angle actuators, which account for critical factors such as wear, hydraulic oil leakage, and external disturbances. Furthermore, simulation models are created to evaluate the system's dynamic response, with particular attention given to the response speed and steady-state error. These models are validated through step and ramp response tests, providing valuable insights into the dynamic performance of multi-pump waterjet propulsion systems.

The structure of this paper is organized as follows: Section 2 outlines the mathematical modeling of the actuators, including the assumptions and derivations used to establish the dynamic models. Section 3 presents the simulation results and analyzes the system's response under different operational conditions, such as wear, leakage, and hydraulic disturbances. Section 4 provides the model validation, where the proposed model's performance is compared against the experimental results. In Section 5, the conclusions summarize the key findings, emphasizing the practical applications of the model in real-world waterjet propulsion systems and suggesting directions for future research.

By offering a detailed analysis of actuator dynamics and validating the models through simulations, this paper contributes a new theoretical foundation for optimizing waterjet propulsion systems. These findings are expected to assist in the design of more precise and efficient control strategies, thereby advancing the capabilities of multi-pump waterjet propulsion technology in maritime applications.

2. Modeling of Actuators in Waterjet Propulsion Systems

2.1. Composition of Actuators in Waterjet Propulsion Systems

The reversing bucket actuator in a waterjet propulsion system consists of several key components, including a main hydraulic pump, a hydraulic power unit (comprising a reservoir and a proportional valve group), an electric pump set, hydraulic accessories, and electrical components, as shown in Figure 1.

The waterjet propulsion system is a complex assembly designed to convert hydraulic energy into thrust for vessel propulsion. The system consists of an inlet duct, pump housing, impeller, stator, nozzle, and control mechanisms. The inlet duct channels water into the pump housing, where the primary pump accelerates the water using an impeller. The stator aligns the water flow before it is expelled through the nozzle to generate thrust. Actuators control the rudder angle and reversing bucket, enabling precise maneuverability.

A hydraulic cylinder serves as a transmission device that converts hydraulic energy into mechanical energy. Dynamic simulation of hydraulic cylinders is essential for analyzing the performance metrics and optimizing the design by modeling their behavior within hydraulic systems. This simulation process typically involves establishing mathematical

models for the hydraulic system, solving the system's motion equations, and simulating the system's dynamic responses.

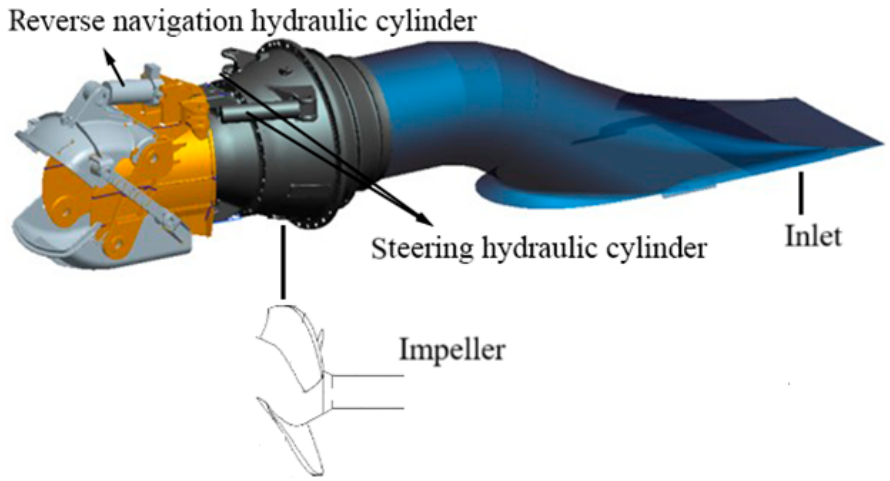


Figure 1. Waterjet propulsion unit.

To conduct a dynamic simulation of hydraulic cylinders, it is first necessary to define the operating conditions and parameters of the hydraulic system. These parameters include the properties of the hydraulic fluid, the structural dimensions of the hydraulic cylinder, and the applied working load. Based on fundamental principles such as the ideal gas law and hydraulic transmission equations, a dynamic model of the hydraulic system can then be established. Solving the dynamic motion equations of the model yields the hydraulic cylinder's dynamic responses, such as position, velocity, and acceleration.

By simulating the dynamic behavior of hydraulic cylinders, we gain a deeper understanding of the operating principles and characteristics of hydraulic systems, enabling us to identify and address potential issues preemptively. Moreover, simulation facilitates the evaluation of hydraulic cylinder performance metrics, including response time, accuracy, and energy consumption, providing a valuable reference for optimizing system structures and control algorithms.

The waterjet propulsion system acts as the primary power and control unit for waterjet-driven vessels. It consists of two main mechanisms: the rudder angle actuator and the reversing bucket actuator. These systems are controlled by proportional valves that regulate the hydraulic actuators, enabling the required maneuvers. To simplify the mathematical derivation of the system model, several secondary factors with minimal impact are disregarded. The following assumptions are made:

(1) The proportional valves are ideal zero-lap four-way spool valves with matched and symmetrical throttling windows.

(2) The flow through the throttling windows is turbulent, while internal and external leakage in the hydraulic cylinder is laminar. The compressibility of the hydraulic fluid within the valve is neglected.

(3) The valves exhibit ideal response behavior.

(4) The supply pressure is constant, and the return pressure is zero.

(5) Pipeline losses and the dynamic behavior of the pipelines are ignored.

(6) All connecting pipelines are assumed to be short and thick, neglecting friction losses, fluid mass effects, and pipeline dynamics.

(7) The pressure in each working chamber of the hydraulic cylinder is uniform, and both the oil temperature and bulk modulus of elasticity are considered constants.

(8) Internal and external leakages within the hydraulic cylinder are laminar flows.

2.2. Valve-Controlled Hydraulic Cylinder Model

Both the rudder angle and reversing bucket actuators use valve-controlled hydraulic cylinders as actuating mechanisms. The rudder angle actuator operates as a parallel control mechanism composed of two asymmetric hydraulic cylinders controlled by a proportional valve, forming a force couple equivalent to a symmetric hydraulic cylinder. In contrast, the reversing bucket actuator consists of a single asymmetric hydraulic cylinder controlled by a proportional valve. Since valve-controlled symmetric hydraulic cylinders represent a special case of valve-controlled asymmetric hydraulic cylinders, a general model for valve-controlled hydraulic cylinders is established using asymmetric cylinders as an example.

(1) Force balance equation between the hydraulic cylinder and the load

According to hydraulic control system theory, and neglecting nonlinear friction forces, A_1, A_2 are the areas of the rodless and rodded chambers of the hydraulic cylinder (m^2);

At steady-state conditions, the force balance equation can be simplified to

$$A_1(p_1 - n_1 p_2) = F_{L0} \tag{1}$$

where

A_1 is the area of the rodless of the hydraulic cylinder (m^2);

p_1, p_2 are the pressures in the rodless and rodded chambers (N/m^2);

n_1 represents the area ratio of the rodded chamber piston to the rodless chamber piston of the hydraulic cylinder;

F_{L0} is the load force acting on the hydraulic cylinder (N).

The load pressure of an asymmetric hydraulic power mechanism is

$$p_L = p_1 - n_1 p_2 \tag{2}$$

(2) Flow continuity equation for the spool valve

The flow through a proportional valve assumes that the spool displacement is either positive or negative.

In steady-state conditions, the flow equation for the proportional valve can be simplified as follows:

$$q_L = K_q^* x_v - K_c^* p_L \tag{3}$$

where

K_q^* is the flow gain of the proportional valve (m^2/s);

K_c^* is the flow-pressure coefficient of the valve (m^5/N).

x_v is the spool displacement (m); p_L is the load pressure (N/m^2).

$$K_q^* = a_1\sqrt{p_s - p_L} + a_2\sqrt{n_1 p_s + p_L} \tag{4}$$

$$K_c^* = a_1 x_v/(2\sqrt{p_s - p_L}) - a_2 x_v/(2\sqrt{n_1 p_s + p_L}) \tag{5}$$

and

$$a_1 = \begin{cases} C_d w\sqrt{\frac{2}{\rho}\frac{1}{n_1^3+1}} & x_v > 0 \\ 0 & x_v < 0 \end{cases}, \alpha_2 = \begin{cases} 0 & x_v > 0 \\ C_d w\sqrt{\frac{2}{\rho}\frac{1}{n_1^3+1}} & x_v < 0 \end{cases}$$

where

C_d is the flow coefficient of the spool valve;

w is the area gradient of the spool valve (m^2);

p_s is the supply pressure (N/m^2).

(3) Flow continuity equation of a hydraulic cylinder

Taking into account the compressibility of hydraulic oil and the internal and external leakage of the hydraulic cylinder and assuming that the piston of the hydraulic cylinder undergoes a minute movement at a certain position $V_{10} = V_{20} = V_0$, the flow continuity equations for the two chambers of the hydraulic cylinder can be expressed as:

$$q_1 = A_1 y + C_{ic}(p_1 - p_2) + C_{ec} p_1 + \frac{V_0}{\beta_e} \dot{p}_1 \tag{6}$$

$$q_2 = A_2 \dot{y} + C_{ic}(p_1 - p_2) - C_{ec} p_2 - \frac{V_0}{\beta_e} \dot{p}_2 \tag{7}$$

where

C_{ic} is the effective area of the hydraulic cylinder piston (m^2);
C_{ec} is the displacement of the hydraulic cylinder piston (m);
V_0 is half of the total volume of the hydraulic cylinder (m^3);
β_e is the equivalent bulk modulus of elasticity of the hydraulic oil (N/m^2).
From Equations (2), (6) and (7), we obtain:

$$q_1 + n_1 q_2 = (1 + n_1^2) A_1 \dot{y} + C_{ic}(p_1 + p_2)(1 + n_1) + C_{oc} p_L + \frac{V_0}{\beta_e} \dot{p}_L \tag{8}$$

Based on the previous derivation, we obtain:

$$\frac{q_1 + n_1 q_2}{1 + {n_1}^2} = A_1 \dot{\nu} + \frac{1 + n_1}{1 + {n_1}^3} C_{ic} p_L + \frac{1}{1 + {n_1}^2} C_{ec} p_L + \frac{V_0}{\beta_e (1 + {n_1}^2)} \dot{p}_L + \frac{1 + n_1}{1 + {n_1}^2} C_{ic} b p_s \tag{9}$$

The last term in the above equation is a constant.
Let

$$q_L = \frac{q_1 + n_1 q_2}{1 + {n_1}^2}$$

$C_{ica} = \frac{1 + n_i}{1 + {n_1}^3} C_{ic}, C_{eca} = \frac{C_{ec}}{1 + {n_1}^2}$, then

$$q_L = A_1 \dot{y} + C_{ıc} p_L + \frac{V_0}{\beta_e (1 + {n_1}^2)} \dot{p}_L + \frac{1 + n_1}{1 + {n_1}^2} C_{ic} b p_s \tag{10}$$

where $C_{tc} = C_{ica} + C_{eca}$.

(4) Transfer function and block diagram

Assuming that the flow through the spool valve is approximately equal to the load flow of the hydraulic cylinder, applying Laplace transforms to Equations (3) and (10) yields the following results:

$$A_1 p_L = m s^2 y + B_c s y + K y + F \tag{11}$$

$$q_L = K_q^* x_v - K_c^* p_L \tag{12}$$

$$q_L = A_1 s y + C_{ıc} p_L + \frac{V_0}{(1 + {n_1}^2) \beta_e} s p_L \tag{13}$$

From these equations, we can derive the block diagram of the valve-controlled hydraulic cylinder, as shown in Figure 2. The block diagram was created and implemented using MWorks Ver 6.02, a modeling and simulation software provided by Tongyuan Co. (Suzhou, China) In the diagram, the valve coefficients K_q^* and K_c^* vary with the directions of the hydraulic cylinder's motion; the system exhibits different dynamic characteristics depending on the movement direction.

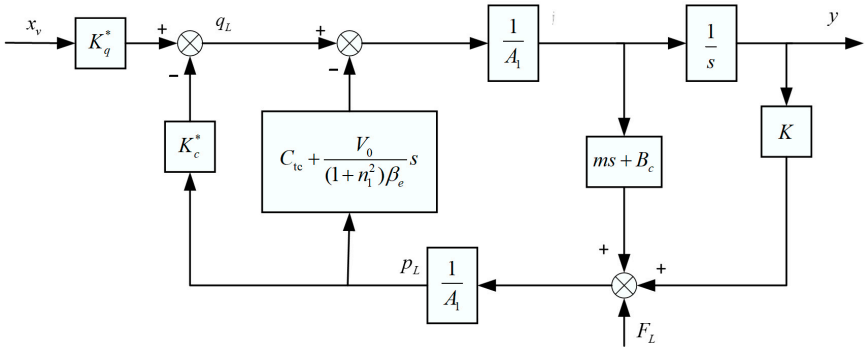


Figure 2. Block diagram of valve-controlled asymmetric cylinder.

From the block diagram, the dynamic characteristic equation for the output variable y is obtained as follows:

$$y = \frac{\frac{K_q^*}{A_1}x_v - \frac{K_{ce}^*}{A_1^2}(\frac{V_0}{(1+{n_1}^2)\beta_e K_{ce}^*}+1)F}{\frac{mV_0}{(1+{n_1}^2)\beta_e {A_1}^2}s^3 + (\frac{mK_{ce}^*}{{A_1}^2}+\frac{B_c V_0}{(1+{n_1}^2)\beta_e {A_1}^2})s^2 + (\frac{KV_0}{(1+{n_1}^2)\beta_e {A_1}^2}+\frac{B_c K_{ce}^*}{{A_1}^2}+1)s+\frac{KK_{ce}^*}{{A_1}^2}} \quad (14)$$

In the formula, $K_{ce}^* = K_c^* + C_t c$.

When the system load consists purely of inertial and viscous components without any elastic elements, we have $K = 0$. Moreover, the parameter $\frac{A_1^2}{K_{ce}^*}$ in the characteristic equation arises from the throttling effect of the valve and leakage in the hydraulic cylinder. Since the value is generally much larger than B_c, the term $\frac{B_c K_{ce}^*}{{A_1}^2}$ can be ignored compared to 1. We have the following:

$$y = \frac{\frac{K_q^*}{A_1}x_v - \frac{K_{ce}^*}{A_1^2}\left(\frac{V_0}{(1+n_1^2)\beta_e K_{ce}^*}s+1\right)F}{s\left(\frac{s^2}{\omega_h^2}+\frac{2\zeta_h}{\omega_h}s+1\right)} \quad (15)$$

In the formula:

$$\omega_h = \sqrt{\frac{(1+n_1^2)\beta_e A_1^2}{mV_0}},\ \zeta_h = \frac{K_{ce}^*}{2A_1}\sqrt{\frac{(1+n_1^2)\beta_e m}{V_0}} + \frac{B_c}{2A_1}\sqrt{\frac{V_0}{(1+n_1^2)\beta_e m}}.$$

The generalized transfer function in Equation (15) for a valve-controlled asymmetric hydraulic cylinder applies to various configurations. When $n_1 = 1$, Equation (15) represents the transfer function for a symmetric valve controlling a symmetric cylinder. When $0 < n_1 < 1$, it represents the transfer function for a symmetric valve controlling an asymmetric cylinder.

(5) Determination of hydraulic natural frequency

The transfer function model and block diagram of the dynamic system were derived with several simplifications and assumptions. However, as operating conditions change, the main performance parameters of the system may also change. It is crucial to accurately calculate and appropriately determine these parameters when applying the transfer function model in system analysis and engineering design.

When the hydraulic cylinder piston rod is connected to an inertial load with an equivalent mass, it forms a hydraulic spring–mass system. The natural frequency of this system depends on the position of the piston. The hydraulic cylinder behaves like a highly

stiff linear spring, with its total stiffness being the sum of the hydraulic spring stiffnesses generated by the compressed fluid in each chamber. The total hydraulic spring stiffness K_h can be expressed as:

$$K_h = \beta_e \left(\frac{A_1^2}{V_1} + \frac{A_2^2}{V_2} \right) \tag{16}$$

where

K_h is the hydraulic spring stiffness (N/m);

V_1 and V_2 are the effective volumes of the rodless and rodded chambers of the hydraulic cylinder (m^3);

Ignoring the effects of dead volume in the hydraulic cylinder and the pipe volumes between the valve and the two chambers, we have:

$$V_1 = A_1 y_0 \tag{17}$$

$$V_2 = A_2 (L - y_0) \tag{18}$$

From Equations (23) to (25), we obtain:

$$K_h = \beta_e \left(\frac{A_1}{y_0} + \frac{A_2}{L - y_0} \right) \tag{19}$$

From this expression, we can find that when K_h takes its minimum value,

$$y_0 = \frac{L}{1 + \sqrt{n_1}} \tag{20}$$

At this point, the minimum value $K_{h\min}$ of the hydraulic spring stiffness K_h is:

$$K_{h\min} = \beta_e \frac{(1 + \sqrt{n_1})^2 A_1}{L} \tag{21}$$

The lowest hydraulic natural frequency of the system can be determined as follows:

$$\omega_h = \sqrt{\frac{K_{h\min}}{m}} = (1 + \sqrt{n_1}) \sqrt{\frac{\beta_e A_1}{mL}} \tag{22}$$

The above analysis shows that the lowest hydraulic natural frequency of an asymmetric hydraulic cylinder occurs at the position of $y_0 = \frac{L}{1 + \sqrt{n_1}}$. This frequency is lower than the hydraulic natural frequency calculated using Equation (29). Therefore, the transfer function derived earlier for the valve-controlled hydraulic cylinder, except in the case of a symmetric valve controlling a symmetric cylinder, does not correspond to the lowest hydraulic natural frequency.

In engineering design, to ensure system stability, it is recommended to use the lowest hydraulic natural frequency calculated from Equation (22). Alternatively, an empirical formula can be applied to estimate this frequency:

$$\omega_h = \sqrt{\frac{2\beta_e (A_1 + A_2)}{mL}} \tag{23}$$

It is also important to note that the position where the hydraulic spring stiffnesses generated by the compressed liquid in the two chambers of an asymmetric cylinder is equal ($y_{h0} = \frac{L}{1 + n_1}$) and does not coincide with the position of the lowest hydraulic natural

frequency of the hydraulic cylinder ($y_0 = \frac{L}{1+\sqrt{n_1}}$). This differs from the symmetric cylinder case, where both the stiffness and the lowest frequency occur at the midpoint of the piston stroke.

(6) Selection of hydraulic damping ratio

The damping ratio ζ_h is a critical parameter that can vary significantly depending on the operating conditions. It is often considered a "soft" parameter, as it is difficult to determine precisely. Nonlinear friction in the system can introduce additional damping, particularly when the hydraulic cylinder operates near its zero position, where the piston movement is minimal. Additionally, as the valve opening increases, the increased flow through the valve also contributes to a rise in the damping ratio.

However, the damping ratio calculated using standard expressions may underestimate the actual damping effect, particularly under varying working conditions. Therefore, the selection of an appropriate damping ratio should account for both the specific operating conditions and the working environment of the dynamic system. Practical experience plays an essential role in fine-tuning this parameter.

In general, for engineering applications, a damping ratio ζ_h in the range of 0.1 to 0.2 is often considered adequate to ensure system stability and a satisfactory dynamic response.

2.3. Model of the Reversing Bucket Actuator for the Waterjet Propulsion System

The reversing bucket actuator in the waterjet propulsion system consists of two plates connected by a linkage mechanism at both the upper and lower parts of the bucket. These plates can open and close, functioning similarly to an anchor. To facilitate smooth operation, two arms are mounted on the vertical cross-section of the nozzle for rotary motion. Horizontal levers connect these arms to a hydraulic cylinder positioned at the top of the nozzle. When the vessel is operating in forward mode, the upper plate of the reversing bucket remains horizontal, parallel to the bottom of the steering nozzle. In reverse mode, the water jet from the pump is deflected by the reversing bucket towards the front and lower direction of the bow, generating reverse thrust. However, when the reversing bucket is positioned at the exact center, the water jet does not produce any thrust on the vessel, regardless of pump speed, resulting in zero thrust.

The relationship between the angular displacement α_d of the reversing bucket actuator's nozzle and the displacement y of the actuator's hydraulic cylinder is expressed as:

$$\alpha_d = K_1 y \tag{24}$$

where

α_d is the swing angle of the reversing bucket actuator's nozzle (rad);

K_1 represents the proportional relationship between the swing angle of the actuator's nozzle and the hydraulic cylinder's displacement (rad/m).

The dynamic characteristics of the proportional valve in the waterjet propulsion system can be modeled as a second-order oscillatory system:

$$G_{vd}(s) = \frac{K_{vd}\omega_{nvd}^2}{s^2 + 2\xi_{nvd}\omega_{nvd}s + \omega_{nvd}^2} \tag{25}$$

where

K_{vd} is the gain relating the input current to the spool displacement of the control proportional valve (m/A);

ω_{nvd} is the natural frequency of the proportional valve (rad/m);

ξ_{nvd} is the damping ratio of the proportional valve.

The response frequency of the proportional amplifier is relatively high, allowing it to be modeled as a proportional element:

$$K_{ad} = \frac{i_d}{U_d} \tag{26}$$

where

K_{ad} is the gain of the proportional amplifier (A/V);

i_d is the input current to the control valve (A);

U_d is the output voltage of the controller (V).

The displacement sensor in the reversing bucket actuator control system has a high response frequency and can also be modeled as a proportional element:

$$K_{fd} = \frac{U_{fd}}{y} \tag{27}$$

where

K_{fd} is the amplification factor of the displacement sensor (V/m);

U_{fd} is the output voltage of the displacement sensor (V).

Since the dynamic mechanism of the reversing bucket actuator is a valve-controlled asymmetric cylinder, and the stiffness of the elastic load is assumed to be large enough to be negligible, the transfer function of the dynamic mechanism can be simplified as:

$$y = \frac{\frac{K_{qd}}{A_1}x_v - \frac{K_{ced}}{A_1^2}\left(\frac{V_0}{(1+n_1{}^2)\beta_e K_{ced}}s + 1\right)F}{s\left(\frac{s^2}{\omega_{hd}{}^2} + \frac{2\zeta_{hd}}{\omega_{hd}}s + 1\right)} \tag{28}$$

where K_{qd} and K_{ced} correspond to K_q^* and K_{ce}^* defined in Equation (15), respectively.

Based on the transfer function models of the above components, the block diagram of the reversing bucket actuator control system is depicted in Figure 3.

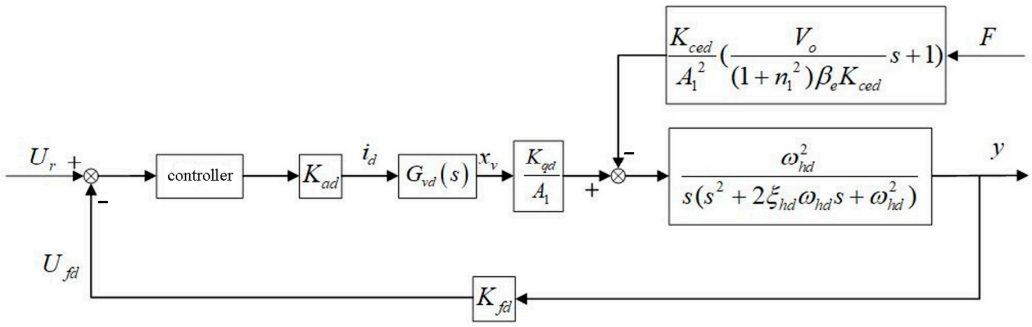


Figure 3. Block diagram of the reversing bucket actuator control system.

From the block diagram in Figure 3, the transfer function between the desired hydraulic cylinder stroke command and the actual hydraulic cylinder stroke can be derived as:

$$G_d(s) = \frac{K_1 K_{ad} K_{fd} \frac{K_{qd}}{A_1} G_{vd}(s)}{s\left(\frac{s^2}{\omega_{hd}{}^2} + \frac{2\xi_{hd}}{\omega_{hd}}s + 1\right)} \tag{29}$$

In a semi-physical simulation, the transfer function of the reversing bucket actuator has two inputs and one output. The inputs are the desired angle signal (i.e., the joystick

signal for controlling the reversing bucket) and the disturbance force F from the load piston. The output is the actual angle of the reversing bucket.

2.4. Model of the Rudder Angle Actuator for the Waterjet Propulsion System

In ships using waterjet propulsion, steering and reversing during normal navigation are primarily achieved by adjusting the nozzle angle of the waterjet pump according to navigational needs, thereby changing the direction of the water jet. A typical rudder angle actuator system, which includes components such as a steering nozzle, hydraulic cylinders, high-pressure hoses, and feedback control mechanisms, enables this functionality. The steering nozzle can typically rotate up to 30 degrees to the left or right, depending on the navigational requirements of the ship. The hydraulic cylinder responsible for adjusting the nozzle is connected to the hydraulic system via high-pressure hoses.

The rudder angle actuator utilizes a parallel control mechanism comprising two asymmetric hydraulic cylinders working in opposition to form a couple effect. This configuration allows the two asymmetric cylinders to be modeled as an equivalent single symmetric hydraulic cylinder, with $n_1 = 1$ in the generalized valve-controlled hydraulic cylinder model. Therefore, the transfer function for the valve-controlled hydraulic cylinder in the rudder angle actuator is given by:

$$y_c = \frac{\frac{K_{qc}}{A} x_v - \frac{K_{cec}}{A}\left(\frac{V_t}{4\beta_e K_{cec}} s + 1\right) F_c}{s\left(\frac{s^2}{\omega_{hc}^2} + \frac{2\zeta_{hc}}{\omega_{hc}} s + 1\right)} \tag{30}$$

where

y_c represents the displacement of the hydraulic cylinder in the rudder angle actuator (m);

K_{qc} is the flow gain of the control proportional valve spool ($m^3/s/A$);

A is the effective total area of the hydraulic cylinder piston (m^2);

K_{cec} is the sum of the total leakage coefficient and valve flow-pressure coefficient of the hydraulic cylinder of the rudder angle actuator ($m^5/(N \times s)$);

V_t is the total volume of the hydraulic cylinder of the rudder angle actuator (m^3);

F_c is the external load force controlled by the rudder angle actuator (N);

ω_{hc} is the hydraulic natural frequency of the rudder angle actuator (rad/s);

ζ_{hc} is the hydraulic damping ratio of the rudder angle actuator.

The relationship between the nozzle angle of the rudder angle actuator and the displacement of the hydraulic cylinder can be described as:

$$\alpha_c = K_2 y_c \tag{31}$$

where

α_c is the swing angle of the nozzle of the rudder (rad);

K_2 is the linear relationship between the swing angle of the nozzle and the displacement of the hydraulic cylinder (rad/m).

The proportional amplifier used in the control system has a high response frequency and can be modeled as a proportional element:

$$K_{ac} = \frac{i_c}{u_c} \tag{32}$$

where

K_{fc} is the amplification factor of the displacement sensor (V/m);

U_{fc} is the output voltage of the displacement sensor (V).

Based on the transfer function models of the above-mentioned elements, the block diagram of the rudder angle actuator control system is shown in Figure 4.

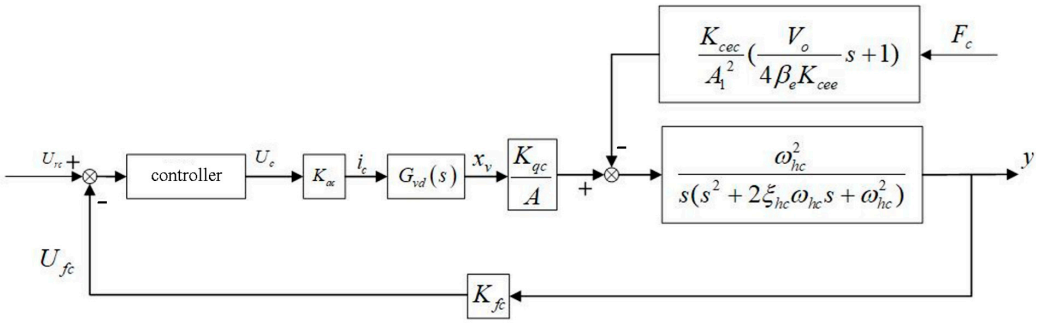


Figure 4. Block diagram of the rudder angle actuator control system.

From this block diagram, when the controller is a proportional control unit, the open-loop transfer function between the commanded rudder angle hydraulic cylinder stroke and the actual rudder angle hydraulic cylinder stroke for the rudder angle actuator control system is:

$$G_c(s) = \frac{K_2 K_{ac} K_{fc}(\frac{K_{qc}}{A}G_{vd}(s) - \frac{K_{cec}}{A^2}(\frac{V_t}{4\beta_e K_{cec}}s+1)F_c)}{s(\frac{s^2}{\omega_{hc}^2}+\frac{2\zeta_{hc}}{\omega_{hc}}s+1)} \quad (33)$$

During hardware-in-the-loop simulation, the transfer function for the rudder angle actuator has two inputs and one output. The inputs are the desired rudder angle signal (the joystick command) and the disturbance force FFF from the load piston, while the output is the actual rudder angle signal.

The models and simulations in this study were developed and executed using the MWorks software by Tongyuan Co. MWorks provides a powerful platform for modeling, simulating, and analyzing multidisciplinary dynamic systems, enabling an accurate representation of the waterjet propulsion system and its associated control strategies.

3. Results

3.1. Simulation Results of Waterjet Propulsion Devices

The parameters of the waterjet propulsion system, including those of the reversing bucket and rudder angle actuator parameters, are summarized in Tables 1–4.

Table 1. Parameters of the reversing bucket.

Cylinder Bore Diameter	180 mm	Piston Rod Diameter	100 mm
Forward Chamber Cross-Sectional Area	17,592.9 mm^2	Reverse Chamber Cross-Sectional Area	25,449.9 mm^2
Maximum Flow Rate of Proportional Valve	76 L/min	Deadband of Proportional Valve	0~±5%

Table 2. Comparison of hydraulic cylinder piston stroke and reversing angle.

Angle of the Reversing Bucket Jaw (°)	0	5	10	15	20	25	30	35	40	45
Stroke of the Reversing Cylinder (mm)	0	44	82	115	144	170	191	211	229	244

Table 3. Steering parameters.

Cylinder Bore Diameter	140 mm	Piston Rod Diameter	80 mm
Cross-Sectional Area of Chamber with Rod	10,367.3 mm^2	Cross-Sectional Area of Chamber without Rod	15,393.8 mm^2
Cross-Sectional Area of Left/Right Steering Hydraulic Chamber	25,761.1 mm^2	Deadband of Proportional Valve	0~±5%

Table 4. Comparison of piston stroke and rudder angle.

Rudder Angle (°)	0	5	10	15	20	25	30
Single-sided Stroke of Steering Hydraulic Cylinder (mm)	0	40	80	119	157	195	232

Based on these parameters and considering the deadband, angle–stroke relationships, and maximum stroke, the block diagrams for the control systems governing the commanded versus actual angles of the reversing bucket and rudder angle actuators are illustrated in Figure 5.

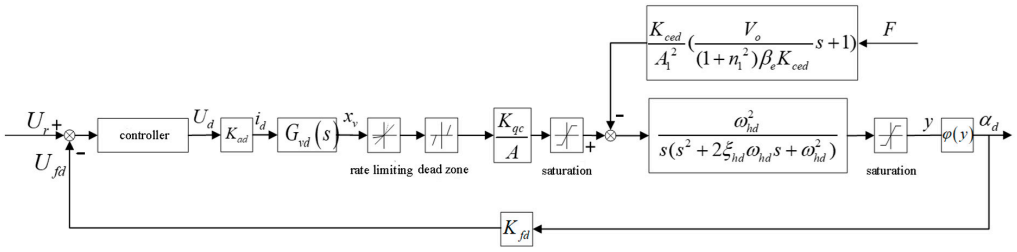


Figure 5. Block diagram of the control system for the reversing bucket actuator.

In the diagram, $\alpha_e = \varphi(y)$ represents the relationship between the piston stroke and the angle of the reversing bucket, fitted based on Table 2. $\alpha_e = \varphi'(y)$ represents the relationship between the piston stroke and the rudder angle, fitted based on Table 4. Using the system parameters and the previously developed model, the hydraulic servo system model for the waterjet propulsion device is illustrated in Figure 6.

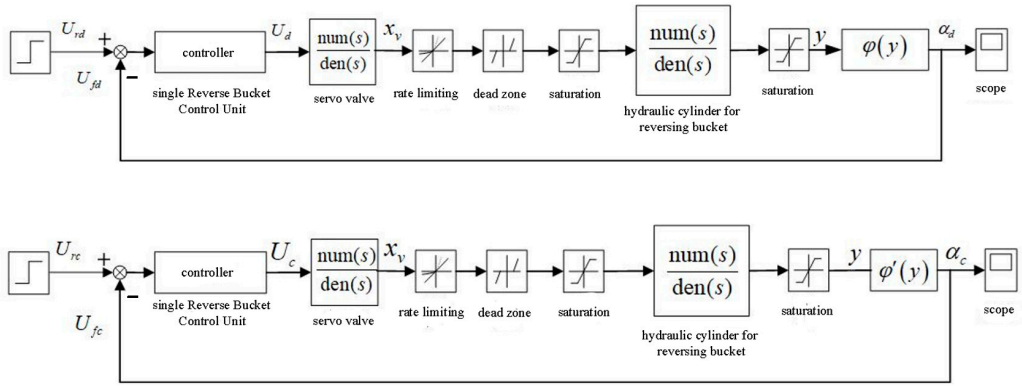


Figure 6. Hydraulic servo system model for waterjet propulsion devices.

Variations in production processes and installation conditions lead to differences in the dynamic characteristics of reversing bucket actuators and rudder angle mechanisms. Furthermore, during operation, these actuators influence the water flow state, affecting the hydrodynamic performance of neighboring actuators. To address these inconsistencies, a coordinated control method is proposed to reduce the discrepancies among actuators, enhancing the overall consistency of the reversing bucket and rudder angle mechanisms.

To assess the performance of the control system, PID controllers were designed for each rudder angle actuator. A ramp response test was then conducted, where the input was the desired rudder angle (joystick signal) and the actual feedback from a sensor. The output was the control input for the rudder angle actuator in the next cycle. When the ramp signal amplitude for the rudder angle actuator was set to 60°, we obtained the response curve shown in Figure 7.

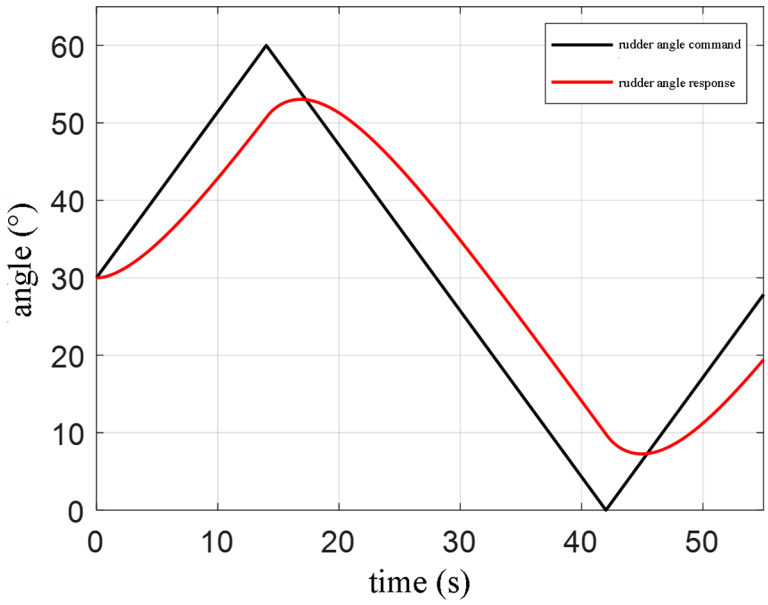


Figure 7. Ramp response of the rudder angle actuator.

A corresponding PID controller was designed for the reversing bucket actuator, and a ramp response test was conducted. In the PID controller, the input consisted of the desired reversing bucket angle and the actual feedback value, while the output was the control input for the next cycle. When the ramp signal amplitude was set to 45°, we obtained the response curve presented in Figure 8.

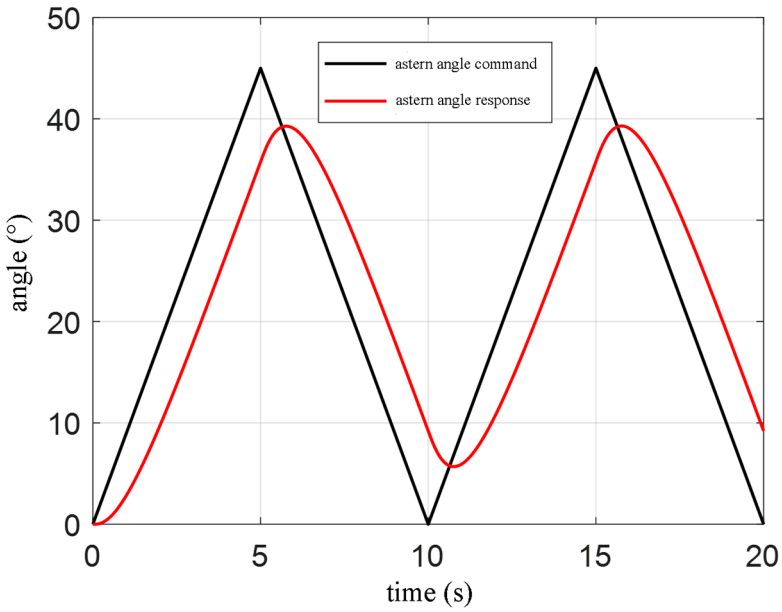


Figure 8. Ramp response of the reversing bucket actuator.

The phase lag that was observed between the astern angle command and response is primarily attributed to the combined effects of system inertia and the hydraulic servo system's intrinsic delay. The proportional valve's deadband, which ranges from 0 to ±5%, also contributes to the delayed response as the system compensates to overcome the initial unresponsiveness. Interestingly, the phase lag diminishes as the system approaches steady-state conditions, reflecting effective PID tuning.

The simulation results demonstrate that the established models of the rudder angle and reversing bucket actuators exhibit rapid response times with no steady-state errors. This indicates that the designed single-loop control systems meet the performance requirements for the waterjet propulsion units. The mathematical modeling and single-cylinder closed-loop simulations provide a solid foundation for the development and experimental validation of automatic zero-position calibration systems and multi-pump coordination control systems for waterjet propulsion devices.

3.2. Dynamic Characteristic Analysis and Simulation of Waterjet Propulsion Systems

3.2.1. Analysis of Wear, Leakage, and Hydraulic Oil Pressure Disturbances

The wear observed in hydraulic cylinders is influenced by factors such as the wear resistance of the cylinder material and the presence of external load particles. Abrasive wear is the dominant type of internal wear failure in hydraulic cylinders, and it is a significant contributor to overall wear-related failures. This type of wear is characterized by visible abrasion marks inside the cylinder body, which can negatively affect the pressure generated by the hydraulic oil. When wear occurs in the actuator, its dynamic response deteriorates, leading to a slower response, reduced overshoot, and prolonged adjustment times. The analysis shows that wear primarily affects the deadband range of the actuator, which corresponds to the deadband percentage D in the deadband component of the system model.

It is important to note that while this analysis focuses on the primary effects of wear, such as the material properties and the internal wear mechanisms, external condition fluctuations—such as variations in temperature, humidity, or dynamic external loads—can also influence wear behavior and its impact on actuator dynamics. These external factors are not explicitly considered in this study to maintain a manageable scope and computational focus. Future studies will extend the model to incorporate these variables for more comprehensive predictions.

Hydraulic oil leakage can impact hydraulic cylinders in multiple ways, depending on the location and extent of the leak, as well as the overall design of the hydraulic system. Some of the major consequences include:

- Reduced System Efficiency: Oil leaks can lead to a drop in system pressure, which in turn lowers the overall efficiency of the hydraulic system. As the amount of oil leakage increases, system efficiency diminishes proportionally.
- Degraded Cylinder Performance: Hydraulic cylinders rely on adequate oil pressure to generate the required pushing or pulling force. A leak in the system can result in insufficient oil pressure, causing the cylinders to underperform, which may manifest as a loss of force or reduced speed.
- Increased Maintenance Costs: Leaks necessitate more frequent refills to compensate for lost hydraulic oil, leading to higher operational costs. Additionally, persistent leaks may require component repairs or replacements, further increasing system maintenance costs.

When hydraulic oil leakage occurs in the actuator, its dynamic characteristics are altered due to the loss of oil pressure, resulting in reduced output. Analysis suggests that oil leakage mainly affects the gain of the system, which corresponds to certain parameters

(such as K_{vd} and K_{qc}) in the model. By adjusting these parameters, it is possible to simulate different leakage rates and their impact on system performance.

3.2.2. Analysis of the Impact of Actuator Wear on Control Performance

Actuator wear primarily affects the deadband range of the mechanism, which corresponds to the deadband percentage DDD in the model. In this analysis, a ramp response input is applied to assess the impact of different levels of wear on the actuator's performance. By adjusting the deadband percentage based on the values provided in Tables 5 and 6, the simulated response curves for the rudder angle and reversing bucket actuators under various wear conditions are shown in Figures 9 and 10, respectively.

Table 5. Simulation results of wear conditions in the rudder angle actuator.

Multiplier of Deadband Percentage Increase	0	1.2	1.5	2
Dynamic Maximum Deviation (°)	6.85	10.81	14.44	18.36
Settling Time (s)	16.98	19.00	21.80	22.94

Table 6. Simulation results of wear conditions in the reversing bucket actuator.

Deadband Percentage Increase Factor	0	1.2	1.5	2
Dynamic Maximum Deviation (°)	5.68	7.32	8.52	10.20
Settling Time (s)	5.76	5.98	6.30	6.70

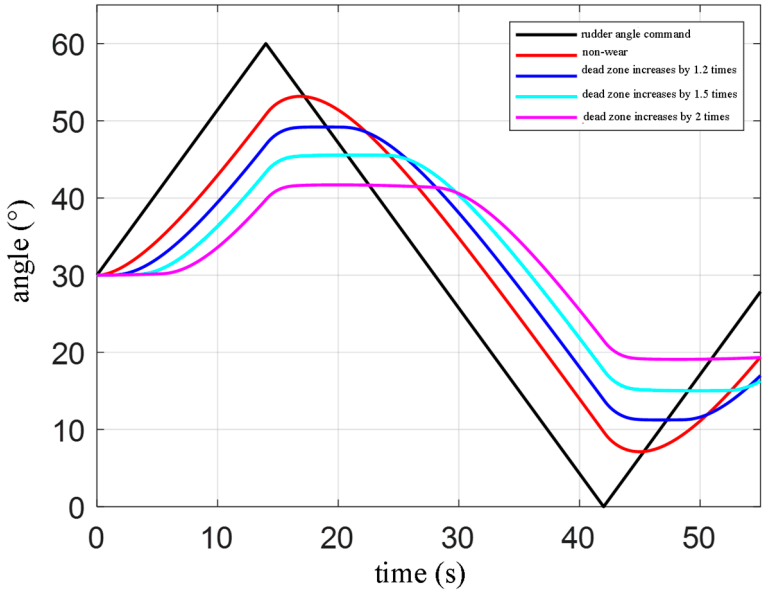


Figure 9. Response curve of the rudder angle actuator under wear conditions.

The phase discrepancy observed in Figure 9 between the input command (desired rudder angle) and the actual response highlights the nonlinear dynamics introduced by wear. This lag can be physically interpreted as the additional time required for the actuator to overcome the expanded deadband before generating sufficient force to achieve the desired motion. The wear also impacts the hydraulic fluid flow within the cylinder, further compounding the response time. The results suggest that wear significantly impacts not only the control performance but also the safety and operational reliability of the waterjet propulsion system. For instance, during high-precision maneuvers or emergency scenarios, the increased settling time and deviation could lead to suboptimal responses, potentially compromising the vessel's handling and stability.

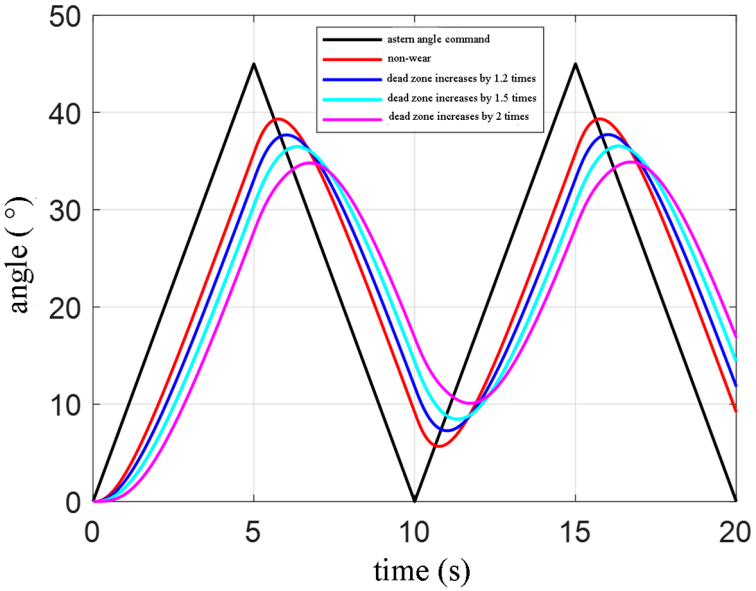


Figure 10. Response curve of the reversing bucket actuator under wear conditions.

Figure 10 demonstrates the impact of an increasing deadband on the steering system's efficiency, highlighting a clear decline as the wear progresses. Efficiency drops from 94.7% under normal conditions to 78.3% at a deadband multiplier of 2. This reduction stems from the energy losses associated with repeated corrections and a prolonged actuator response time. As the deadband widens, the actuator must frequently compensate for inaccuracies, resulting in higher energy consumption and reduced effective output.

The findings emphasize the critical role of precise actuator performance in maintaining system efficiency. A sharp decline in efficiency can significantly affect vessel operation, particularly during prolonged missions where fuel economy and energy management are crucial. Implementing predictive maintenance strategies and advanced control algorithms, such as deadband compensation or energy-efficient optimization, could effectively mitigate these losses, ensuring sustained operational efficiency even under wear conditions.

To further validate these findings, it would be beneficial to compare the simulated results with experimental data or existing literature. For example, studies on hydraulic actuator wear in other marine or industrial systems could provide benchmarks to assess the accuracy and generalizability of the model. Incorporating these comparisons in future work could strengthen the robustness of the conclusions drawn from this study.

Table 5 presents the simulation results for the rudder angle actuator under different levels of deadband increase, while Table 6 shows the corresponding results for the reversing bucket actuator. The deadband percentage increase factor reflects the degree of wear in the actuator, which leads to a larger deadband range and consequently affects the system's dynamic response.

In Table 5, as the deadband percentage increases, the rudder angle actuator exhibits a significant rise in dynamic maximum deviation, from 6.85° at the baseline (no wear) to 18.36° at a deadband increase factor of 2. Similarly, the settling time increases from 16.98 s to 22.94 s, indicating a slower system response due to increased wear.

Table 6 shows a similar trend for the reversing bucket actuator. The dynamic maximum deviation increases from 5.68° at baseline to 10.20° as the deadband percentage increases, while the settling time gradually rises from 5.76 s to 6.70 s. The results demonstrate that wear-induced changes in the deadband range directly affect both the dynamic deviation and settling time, with more pronounced effects observed in the rudder angle actuator compared to the reversing bucket actuator.

These findings highlight the sensitivity of actuator performance to wear, emphasizing the importance of periodic maintenance and recalibration to minimize deadband-related control performance degradation in waterjet propulsion systems.

3.2.3. Simulation of Hydraulic Oil Leakage in the Actuator

Hydraulic oil leakage in the actuator primarily affects the system gain, which corresponds to specific parameters within the model. This leakage reduces the efficiency of the actuator by decreasing the hydraulic pressure, leading to a drop in system responsiveness and control precision. To simulate the effects of hydraulic oil leakage, ramp response inputs are applied under varying leakage conditions for both the rudder angle and reversing bucket actuators. The leakage conditions for the rudder angle actuator are configured based on the data in Tables 7 and 8. The corresponding response curves are shown in Figures 11 and 12, illustrating the impact of hydraulic oil leakage on the dynamic performance of these actuators.

Table 7. Simulation results of leakage in the rudder angle actuator.

Hydraulic Oil Leakage Flow Rate (L/min)	0	3.80	7.60	11.40
Dynamic Maximum Deviation (°)	6.84	9.63	17.00	25.25
Settling Time (s)	16.86	18.26	21.84	25.78

Table 8. Simulation results of leakage in the reversing bucket actuator.

Hydraulic Oil Leakage Flow Rate (L/min)	0	3.80	7.60	11.40
Dynamic Maximum Deviation (°)	5.64	8.43	20.13	35.71
Settling Time (s)	5.74	6.08	7.32	8.46

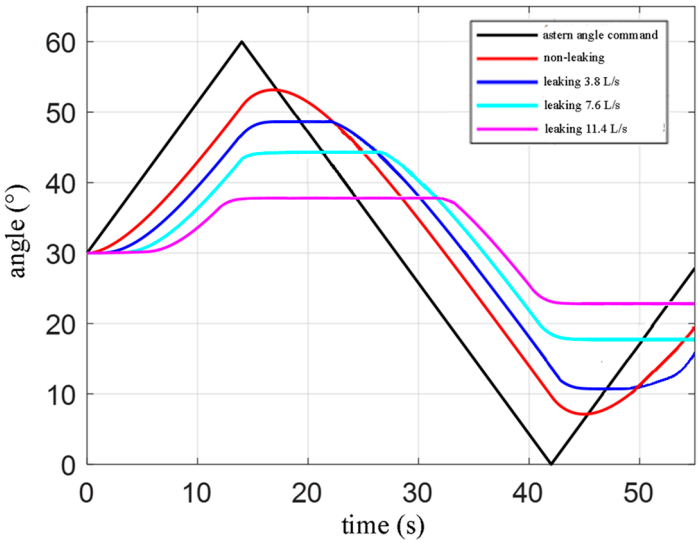


Figure 11. Response curve of the rudder angle actuator under leakage conditions.

Tables 7 and 8 present the simulation results of hydraulic oil leakage on the rudder angle and reversing bucket actuators, respectively. As shown in Table 7, as the leakage flow rate increases, the rudder angle actuator experiences a significant rise in dynamic maximum deviation, from 6.84° at baseline (no leakage) to 25.25° at a leakage flow rate of 11.40 L/min. Similarly, the settling time increases from 16.86 s to 25.78 s, indicating that leakage slows down the actuator's response time due to decreased hydraulic pressure.

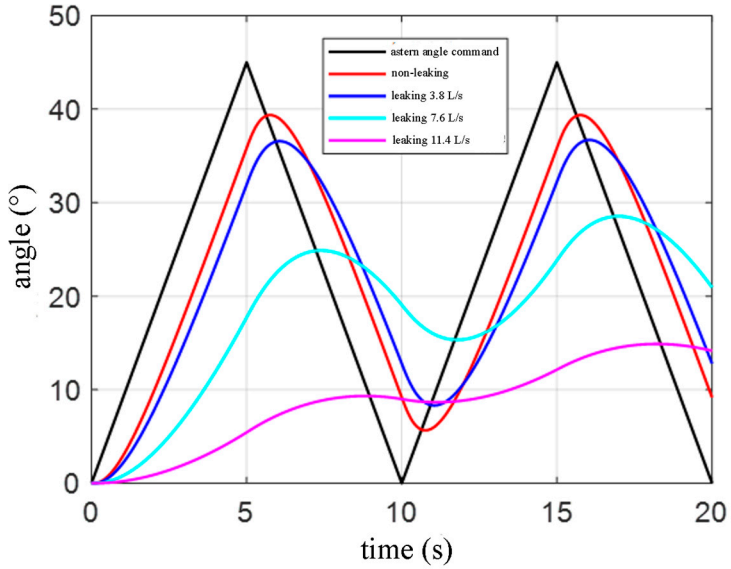


Figure 12. Response curve of the reversing bucket actuator under leakage conditions.

Table 8 shows a comparable trend for the reversing bucket actuator, where the dynamic maximum deviation rises from 5.64° at baseline to 35.71° at a leakage flow rate of 11.40 L/min. The settling time also increases from 5.74 s to 8.46 s, further illustrating the detrimental effects of hydraulic oil leakage on system performance. These results indicate that hydraulic oil leakage has a more pronounced impact on the reversing bucket actuator compared to the rudder angle actuator, particularly at higher leakage flow rates.

It is worth noting that this study focuses on internal factors such as hydraulic oil leakage to establish a foundational understanding of their impact on actuator performance. External environmental factors, including temperature variations, external loads, or other operational conditions, can further influence system behavior and may exacerbate the effects of internal issues such as leakage. These external influences are beyond the scope of this study but are critical for a comprehensive evaluation of actuator performance and system reliability. Future research will extend this work by integrating external factors into the simulation model to better reflect real-world operating environments.

The simulations highlight the critical importance of minimizing hydraulic oil leakage to maintain optimal control performance in waterjet propulsion systems. Leakage not only reduces the actuators' dynamic response but also increases system instability, necessitating more frequent maintenance and potential recalibration of the control parameters.

Although this study does not specify the power of the water jet engine or the characteristics of the vessels, the findings are broadly applicable to medium to large vessels typically powered by water jet engines ranging from 500 kW to 3 MW. Examples include high-speed ferries, patrol boats, and other vessels requiring precision maneuverability. The insights gained from this analysis can be extended to such applications, providing a foundation for further refinement and customization based on specific vessel and engine parameters.

An important parameter in assessing propulsion systems is the transition time from one extreme position to another. While this study focuses on the dynamic deviations and settling times under varying leakage conditions, the transition time can be inferred from the settling times provided in Tables 7 and 8. For instance, under baseline conditions (no leakage), the rudder angle actuator achieves stabilization in approximately 16.86 s, whereas the reversing bucket actuator stabilizes in about 5.74 s. These times increase proportionally with leakage flow rates, emphasizing the adverse impact of leakage on system responsiveness.

3.2.4. Simulation of Hydraulic Oil Disturbance in the Rudder Angle Actuator

Hydraulic oil disturbances in the actuator introduce uncertainties in system gain parameters, which are modeled as noise functions. These disturbances affect the actuator's dynamic performance by altering its response characteristics. Under ramp response input conditions, hydraulic oil disturbance scenarios for the rudder angle actuator are configured based on the data in Tables 9 and 10. The corresponding simulated ramp response curves for both the rudder angle and reversing bucket actuators are shown in Figures 13 and 14, respectively.

Table 9. Simulation results of hydraulic oil disturbance in the rudder angle actuator.

Amplification Factor of Disturbance Amplitude	0	1.20	1.50	2.00
Dynamic Maximum Deviation (°)	7.00	8.37	9.76	11.17
Settling Time (s)	17.14	17.30	17.38	17.42

Table 10. Simulation results of hydraulic oil disturbance in the reversing bucket actuator.

Amplification Factor of Disturbance Amplitude	0	1.20	1.50	2.00
Maximum Dynamic Deviation (°)	5.73	6.99	8.20	9.07
Settling Time (s)	5.74	5.88	5.93	5.97

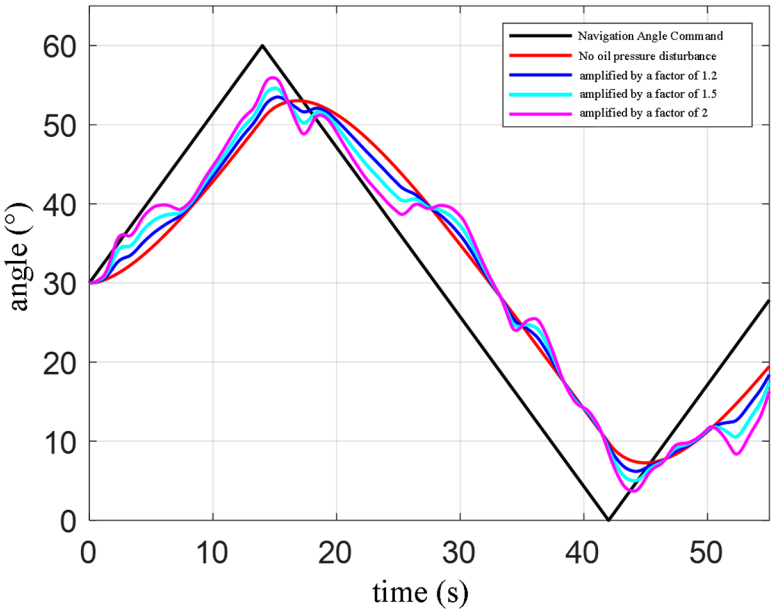


Figure 13. Response curve of the rudder angle actuator under hydraulic oil disturbance.

Figures 13 and 14 present the effects of hydraulic oil disturbances on the dynamic performance of the rudder angle and reversing bucket actuators. As the disturbance amplitude increases, the dynamic maximum deviation in both actuators rises, with the rudder angle actuator showing a more pronounced increase from 7.00° to 11.17° compared to the reversing bucket actuator, which goes from 5.73° to 9.07°. While the maximum deviation increases, the settling time remains relatively stable, indicating that while hydraulic oil disturbances degrade accuracy, they have a limited effect on the overall response time of the system. This suggests that disturbances mainly influence the precision of actuator positioning rather than the speed at which the actuator responds to input commands.

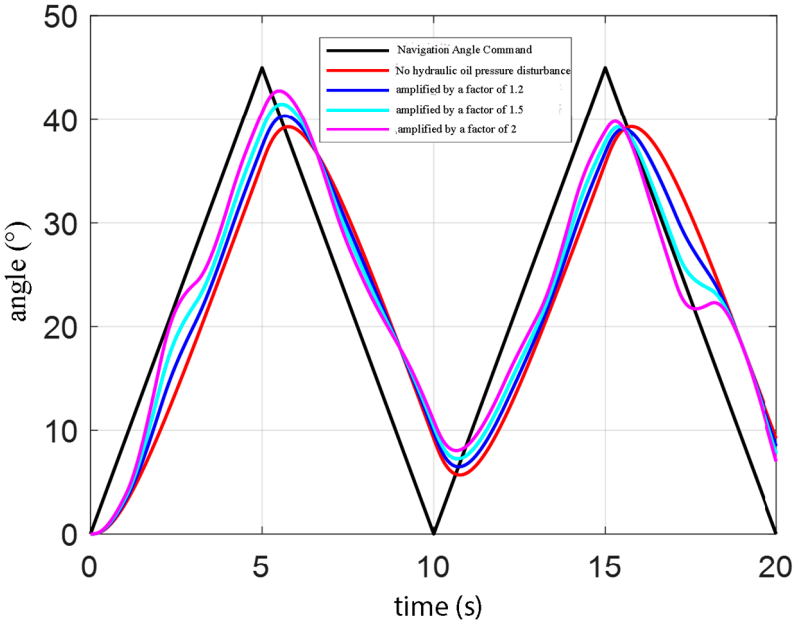


Figure 14. Response curve of the reversing bucket actuator under hydraulic oil disturbance.

The persistent discrepancies in accuracy, particularly under high disturbance conditions, highlight the sensitivity of hydraulic systems to changes in fluid dynamics, such as pressure fluctuations and noise within the hydraulic oil. These disturbances can alter the actuator's gain characteristics, leading to greater control errors and reduced precision in executing desired movements. To mitigate the effects of hydraulic disturbances, incorporating advanced filtering techniques or adaptive control strategies may help to maintain precision by compensating for such disturbances in real time, ensuring a more stable and accurate actuator performance under varying operational conditions.

Tables 9 and 10 summarize the simulation results of hydraulic oil disturbances. In Table 9, we observe that as the disturbance amplitude increases, the dynamic maximum deviation of the rudder angle actuator rises from 7.00° at baseline (no disturbance) to 11.17° at an amplification factor of 2.00. Despite the increasing deviation, the settling time remains relatively stable, increasing only marginally from 17.14 s to 17.42 s. This indicates that while the actuator's precision is affected by hydraulic oil disturbances, its response speed remains relatively unaffected.

Table 10 presents the results for the reversing bucket actuator under similar disturbance conditions. Here, the dynamic maximum deviation increases from 5.73° at baseline to 9.07° at the highest disturbance level. The settling time, like that of the rudder angle actuator, shows minimal change, increasing from 5.74 s to 5.97 s. These results suggest that while hydraulic oil disturbances reduce the accuracy of the actuator, they have a limited impact on the overall response time.

Through the analysis of three typical scenarios—wear in the rudder angle and reversing bucket actuators, hydraulic oil leakage, and hydraulic oil disturbance—this study clarifies the primary influencing factors and their parameter settings in the model. Simulations of these scenarios highlight the operational behavior of the rudder angle and reversing bucket actuators under various conditions, laying the groundwork for designing and experimentally validating multi-pump coordinated control systems for waterjet propulsion devices.

The accurate modeling and control of hydraulic actuators are critical for ensuring precise and reliable operation under varying conditions, including the potential influence of noise in measurement channels. For simplicity, the model assumes ideal measurement

signals without noise interference. However, in practical scenarios, noise in measurement channels can introduce deviations in actuator control, which warrants consideration in control design and simulation validation.

The proposed control strategy achieves a balance between precision and robustness under the tested conditions. While noise in measurement channels was not explicitly modeled, its potential impact on control accuracy can be mitigated by employing filtering techniques or robust control algorithms, ensuring the system's reliability under noisy operational environments. Future work could extend this analysis by explicitly incorporating the influence of measurement noise into the modeling and control framework.

We recognize the importance of model validation and agree that it is crucial to confirm the reliability of our results. Conducting detailed sensitivity analyses and validating models in various operational scenarios will be one of the key focuses of future work.

4. Model Validation of Waterjet Propulsion Device Actuators

The validity of the dynamic models developed for the waterjet propulsion device actuators, particularly the rudder angle and reversing bucket actuators, is a critical aspect of this study. In order to establish the reliability and robustness of these models, it is essential to compare the simulation results with experimental data from real-world actuator performance. Model validation serves as a measure of how well the model predicts the behavior of the system under actual operating conditions. This section provides the necessary steps and methodology for model validation, along with the comparison between experimental data and simulation results, highlighting the discrepancies and evaluation of errors.

For clarity, we define the key variables in our control performance evaluation: the setpoint (SP) is the desired actuator position, the controlled variable (CV) is the actual actuator position, and the manipulated variable (MV) is the control input used to adjust the actuator position. These variables are crucial for evaluating the system's ability to maintain the desired setpoint under various operational conditions. In our analysis, we compare the deviation between the setpoint and controlled variable, and the dynamics of the manipulated variable, which reflect the control system's response. This nomenclature is now consistently used throughout the paper to provide a comprehensive evaluation of control performance.

4.1. Experimental Setup for Model Validation

To perform model validation, real-world experiments were conducted on a marine waterjet propulsion system equipped with both the rudder angle and reversing bucket actuators. The marine waterjet propulsion experimental setup was built by Shanghai Marine Diesel Engine Research Institute (Shanghai, China). The experimental setup included a test rig with the following components:

Test Vessels: A high-speed vessel was equipped with a waterjet propulsion system for real-world actuator performance tests. The vessels were powered by water jet engines ranging from 500 kW to 3 MW, consistent with the typical power ratings for such systems in practical applications.

Hydraulic System: The hydraulic actuators controlling the rudder angle and reversing bucket were instrumented with pressure sensors, flow meters, and position transducers to capture real-time data of the actuator performance.

Control System: The actuators were controlled via a real-time control system, allowing for ramp and step input commands, which are similar to the conditions used in the simulation models. The system was designed to replicate the control environment assumed in the model.

Measurement Equipment: High-precision measurement tools were employed to track the dynamic responses of the actuators, including the dynamic maximum deviation, settling time, and response curve.

All these Data collected from the system under various conditions of actuator wear, hydraulic oil leakage, and disturbances were used to compare the simulation results with real-world performance.

4.2. Experimental Conditions for Model Validation

The experimental conditions were designed to simulate typical wear, leakage, and disturbance scenarios, as outlined in Section 3 of this paper. Specifically, the following conditions were considered:

Wear Conditions: The hydraulic cylinders were subjected to gradual wear, causing an increase in the deadband percentage. The experimental tests were conducted at multiple wear levels, similar to the simulated wear conditions described in Tables 5 and 6. The wear was controlled by introducing fine particles into the hydraulic fluid to simulate the abrasive wear mechanism.

Hydraulic Oil Leakage: The leakage rates varied from baseline (no leakage) to higher leakage flow rates (3.80 L/min, 7.60 L/min, and 11.40 L/min) to mimic real-world leakage scenarios, as described in Tables 7 and 8. The system was monitored for pressure drops and actuator response degradation due to leakage.

Hydraulic Oil Disturbance: Variations in hydraulic oil quality, such as fluctuations in pressure and noise in the fluid, were simulated by introducing disturbances at different amplification factors, as shown in Tables 9 and 10. These disturbances were modeled as random noise functions affecting the system gain and control accuracy.

4.3. Comparison of Simulation and Experimental Data

The simulation results from the models were compared with the experimental data to assess the accuracy of the model predictions. Key parameters such as dynamic maximum deviation, settling time, and response curves were evaluated under the same conditions for both the simulation and experimental setups.

4.3.1. Wear Condition Validation

The simulation results for the rudder angle actuator under various wear levels are shown in Table 5, and the comparison between the simulation and experimental data for the rudder angle actuator is shown in Table 11. The discrepancies between the simulation and experimental results are within an acceptable range, with the largest deviation observed in the maximum deviation angle at the highest wear level (a deadband increase factor of 2). The settling time results show similar trends, with the simulation slightly underestimating the time for stabilization in certain cases.

Table 11. Comparison between the simulation and experimental data for the rudder angle actuator.

Wear Level (Deadband Increase Factor)	Simulation Max Deviation (°)	Experimental Max Deviation (°)	Simulation Setting Time (s)	Experimental Setting Time (s)
0	6.85	7.00	16.98	17.20
1.2	10.81	11.15	19.00	19.30
1.5	14.44	15.10	21.80	22.10
2	18.36	19.25	22.94	23.00

The experimental data for the reversing bucket actuator under different wear conditions (as shown in Table 6) were also compared to the simulation results. Table 12 shows the

comparison. Again, the experimental data closely match the simulated results, with small discrepancies in the maximum deviation and settling time, which are within the expected tolerances for hydraulic systems.

Table 12. Comparison between the simulation and experimental data for the reversing bucket actuator.

Wear Level (Deadband Increase Factor)	Simulation Max Deviation (°)	Experimental Max Deviation (°)	Simulation Setting Time (s)	Experimental Setting Time (s)
0	5.68	5.75	5.76	5.80
1.2	7.32	7.45	5.98	6.05
1.5	8.52	9.10	6.30	6.40
2	10.20	10.50	6.70	6.85

4.3.2. Hydraulic Oil Leakage Validation

For leakage conditions, the experimental data (Tables 7 and 8) were compared with the simulation results. The comparison for the rudder angle actuator is shown in Table 13. The leakage conditions exhibit a reasonable match between the simulation and experimental results. The increasing leakage rate leads to a corresponding rise in both the dynamic deviation and settling time, with slight discrepancies that can be attributed to experimental factors such as leakage measurement accuracy and actuator variability.

Table 13. Comparison between the simulation and experimental data for the hydraulic oil leakage validation.

Leakage Rate (L/mn)	Simulation Max Deviation (°)	Experimental Max Deviation (°)	Simulation Setting Time (s)	Experimental Setting Time (s)
0	6.84	7.05	16.86	17.05
3.8	9.63	10.25	18.26	18.50
7.6	17.00	18.50	21.84	22.10
11.4	25.25	27.00	25.78	26.30

4.3.3. Hydraulic Oil Disturbance Validation

For hydraulic oil disturbance scenarios, a similar comparison was conducted for both the rudder angle and reversing bucket actuators. The simulation results (Tables 9 and 10) were validated with experimental data. For example, the results for the rudder angle actuator with varying disturbance amplitudes are shown in Table 14. The comparison shows that the simulation predictions for the maximum deviation and settling time under disturbance conditions align well with the experimental data. The slight variations are likely due to real-world uncertainties in hydraulic fluid properties and actuator behavior under dynamic conditions.

Table 14. Comparison between the simulation and experimental data for hydraulic oil disturbance validation.

Disturbance Amplification Factor	Simulation Max Deviation (°)	Experimental Max Deviation (°)	Simulation Setting Time (s)	Experimental Setting Time (s)
0	7.00	7.20	17.14	17.32
1.2	8.37	8.50	17.30	17.41
1.5	9.76	9.80	17.38	17.52
2	11.17	11.50	17.42	17.58

The above experiments indicate that the errors for both the maximum deviation and settling time are within acceptable limits, indicating that the simulation models provide reliable predictions of actuator performance under various conditions.

4.4. Discussion of Results

The results of the model validation show that the dynamic models of the rudder angle and reversing bucket actuators accurately reflect real-world actuator behavior. While minor discrepancies exist between the simulation and experimental results, they fall within the expected tolerance for hydraulic systems and actuator response times. The differences can be attributed to real-world factors such as imperfect actuator characteristics, measurement inaccuracies, and slight variations in hydraulic fluid properties.

The validation process demonstrates that the models are effective tools for predicting actuator performance in various operational conditions. This strengthens the foundation for using these models in the design and optimization of waterjet propulsion systems, where actuator performance is critical for efficiency and reliability.

5. Conclusions

This paper presents detailed modeling and analysis of the actuators in marine waterjet propulsion systems, with a focus on dynamic performance under various operational conditions such as actuator wear, hydraulic oil leakage, and hydraulic oil disturbances. The developed models offer valuable insights into actuator behavior and serve as a foundation for the design and optimization of waterjet propulsion systems.

In practical applications, the proposed model can be employed to improve the control performance and reliability of waterjet propulsion systems in real-world scenarios, such as high-speed ferries, patrol boats, and other vessels requiring precise maneuverability. By incorporating the effects of wear and leakage, operators can implement predictive maintenance strategies to minimize performance degradation and ensure safe, efficient operation. Furthermore, the model provides a tool for optimizing control strategies, enabling more responsive and energy-efficient systems, especially in mission-critical operations where reliability and fuel economy are paramount.

Future work will focus on integrating the model into multi-pump coordinated control systems, which can further enhance system performance, robustness, and efficiency. The insights gained from this study contribute to the continued development of advanced marine propulsion technologies and provide a basis for the next generation of waterjet propulsion systems.

Author Contributions: S.J.: Conceptualization, methodology, experimental validation, and drafting of the manuscript. Y.G.: Software development, simulation, data analysis, and drafting of the manuscript. Y.L.: Conceptualization, result analysis, and drafting of the manuscript. D.W.: Software development, data analysis, and experimental validation. C.Q.: Data analysis, experimental validation, and manuscript revision. L.M.: Funding acquisition, conceptualization, data analysis, and manuscript revision. All authors have read and agreed to the published version of the manuscript.

Funding: This research was funded by the Shandong Provincial Natural Science Foundation, grant number ZR2022MH047.

Institutional Review Board Statement: Not applicable.

Informed Consent Statement: Not applicable.

Data Availability Statement: The datasets presented in this article are not readily available because we do not have permission to share the data.

Conflicts of Interest: The authors declare no conflicts of interest.

References

1. Klinger, W.B.; Bertaska, I.; Alvarez, J.; Von Ellenrieder, K.D. Controller design challenges for waterjet propelled unmanned surface vehicles with uncertain drag and mass properties. In Proceedings of the OCEANS 2013 MTS/IEEE—San Diego: An Ocean in Common, San Diego, CA, USA, 23–26 September 2013.
2. Guan, C.; Theotokatos, G.; Zhou, P.; Chen, H. Computational investigation of a large containership propulsion engine operation at slow steaming conditions. *Appl. Energy* **2014**, *130*, 370–383. [CrossRef]
3. Lam, W.; Hamil, G.A.; Song, Y.C.; Robinson, D.J.; Raghunathan, S. A review of the equations used to predict the velocity distribution within a ship's propeller jet. *Ocean Eng.* **2011**, *38*, 1–10. [CrossRef]
4. Carreño, J.E.; Mora, J.D.; Pérez, F.L. Mathematical model for maneuverability of a riverine support patrol vessel with a pump-jet propulsion system. *Ocean Eng.* **2013**, *63*, 96–104. [CrossRef]
5. Han, J.; Xiong, J.; He, Y.; Gu, F.; Li, D. Nonlinear Modeling for a Water-Jet Propulsion USV: An Experimental Study. *IEEE Trans. Ind. Electron.* **2017**, *64*, 3348–3358. [CrossRef]
6. Rebhi, H.; Nejim, S. Modeling and identification of a ship propelled by two water jets. In Proceedings of the 12th International Multi-Conference on Systems, Signals and Devices, SSD 2015, Mahdia, Tunisia, 16–19 March 2015.
7. Eslamdoost, A.; Vikström, M. A body-force model for waterjet pump simulation. *Appl. Ocean. Res.* **2019**, *90*, 101832. [CrossRef]
8. Gong, J.; Wu, Z.; Ding, J.; Jiang, J.; Zhang, Z. Numerical analysis of propulsion performance of a waterjet-propelled vehicle in steady drift. *Ocean Eng.* **2022**, *266*, 113136. [CrossRef]
9. Takai, T.; Kandasamy, M.; Stern, F. Verification and validation study of URANS simulations for an axial waterjet propelled large high-speed ship. *J. Mar. Sci. Technol.* **2011**, *16*, 434–447. [CrossRef]
10. Yang, Q.; Wang, Y.; Zhang, Z. Numerical prediction of the fluctuating noise source of waterjet in full scale. *J. Mar. Sci. Technol.* **2014**, *19*, 510–527. [CrossRef]
11. Ji, G.; Yin, X.; Zhang, Y. Research and analysis of inlet duct cavitation of water jet propulsion. In Proceedings of the 29th International Ocean and Polar Engineering Conference, Honolulu, HI, USA, 16–21 June 2019; 2019; Volume 4, pp. 4768–4773.
12. Liu, X.; Wu, Y.; Zhang, C.; Fan, S. Research on Hydrodynamic Coefficients in Maneuverability of Ship with Water-jet Propulsion. *Ship Build. China* **2023**, *64*, 161–167.
13. Kandasamy, M.; Ooi, S.K.; Carrica, P.; Stern, F. Integral force/moment waterjet model for CFD simulations. *J. Fluids Eng. Trans. ASME* **2010**, *132*, 101103. [CrossRef]
14. Gong, Z.; Li, G.; Xiong, W.; Li, J.; Yu, Y.; Yuan, J. Modeling and simulation of the steering control system of marine water-jet propulsion unit. *Shanghai Jiaotong Daxue Xuebao/J. Shanghai Jiaotong Univ.* **2016**, *50*, 1114–1118.
15. Zhang, H.; Sun, C.; Cai, Y.; Wang, Z. CFD Study on Wake Field of Submerged Waterjet Based on Adaptive Mesh Refinement. *Ship Build. China* **2024**, *65*, 242–249.
16. Zhang, L.; Wei, Y.; Deng, Y.; Yin, H.; Zhang, Y.; Shang, Y.; Zhang, J. A comparative investigation of fixed and free-running CFD self-propulsion models on a waterjet-propelled trimaran. *Ocean Eng.* **2021**, *232*, 109081. [CrossRef]
17. Gong, J.; Dai, Y.-X.; Chen, W. Analysis of Scale Effect on the Propulsion Discrepancy of a Four-Waterjet System. *Ocean. Eng.* **2024**, *308*, 118276. [CrossRef]
18. Gong, J.; Sun, Y.; Ding, J.; Wu, Z.; Zhang, Z. Study on Theoretical Control Volume of Waterjet Propulsion System in Oblique Flow. *Ship Build. China* **2023**, *64*, 24–33.
19. Guo, J.; Meng, K.; Chen, Z.; Feng, Y. CFD-based Optimization of Duct and Nozzle in Waterjet Propulsion System. *Ship Build. China* **2021**, *62*, 97–109.
20. Feng, R.; Liang, T.; Liang, N.; Cao, L.; Wu, D. Numerical simulation of mooring performance of waterjet propulsion system. *Zhejiang Daxue Xuebao (Gongxue Ban)/J. Zhejiang Univ. (Eng. Sci.)* **2024**, *58*, 1050–1059 and 1090.
21. Chen, T.-R.; Liu, H.-R.; Lu, H.; Zhang, X.-P.; Xu, J.; Wang, G.-Y. Performance of Axial Water-Jet Propulsor under Different Inflow Conditions. *Tuijin Jishu/J. Propuls. Technol.* **2023**, *44*, 2211007.
22. Huang, R.; Zhang, R.; Wang, Y.; Luo, X.; Zhu, L. Experimental and numerical investigations into flow features in an intake duct for the waterjet propulsion under mooring conditions. *Lixue Xuebao/Acta Mech. Sin.* **2021**, *37*, 826–843. [CrossRef]
23. Jiang, J.; Ding, J.; Wang, X. A vector control technology of waterjet propelled crafts using synchronous and mirror-equiangular thrust control strategy. *Ocean. Eng.* **2020**, *207*, 107358. [CrossRef]
24. Gong, Z.; Tian, Z.; Xiong, W.; Li, J.; Li, G.; Yuan, J. Global Sliding Mode Control Approach for the Steering System of the Water-Jet Propulsion Device. *Shanghai Jiaotong Daxue Xuebao/J. Shanghai Jiaotong Univ.* **2017**, *51*, 693–697.
25. Tao, R.; Kim, H.; Yoon, H.-J.; Wan, W.; Hovakimyan, N.; Sha, L.; Voulgaris, P. Backup Plan Constrained Model Predictive Control with Guaranteed Stability. *J. Guid. Control. Dyn.* **2024**, *47*, 233–246. [CrossRef]
26. Gong, Z.; Xu, Z.; Lin, H.; Xiong, W.; Liu, T.; Yuan, J. Modelling and synchronous control for a dual-waterjets propulsion steering system. *Trans. Inst. Meas. Control* **2022**, *44*, 144–152. [CrossRef]
27. Lin, F.; Lin, S.; Zeng, S. Co-simulation of neural networks PID control for ship steering hydraulic system. In Proceedings of the 2010 IEEE International Conference on Information and Automation, ICIA 2010, Harbin, China, 20–23 June 2010; pp. 2097–2100.

28. Layne, J.; Passino, K.M. Fuzzy model reference learning control for cargo ship steering. In Proceedings of the 1993 IEEE International Symposium on Intelligent Control, Chicago, IL, USA, 25 August 1993; pp. 457–462.
29. Huo, X.; Hu, J.; Li, Z. BP neural network based PID control for ship steering. In Proceedings of the 2012 World Congress on Information and Communication Technologies, WICT 2012, Trivandrum, India, 30 October–2 November 2012; pp. 1042–1046.
30. Xu, Z.; Gao, S.; Han, Y.; Yuan, J. Modeling and feedback linearization based sliding mode control of diesel engines for waterjet propulsion vessels. *Control. Eng. Pract.* **2020**, *105*, 104647. [CrossRef]

Disclaimer/Publisher's Note: The statements, opinions and data contained in all publications are solely those of the individual author(s) and contributor(s) and not of MDPI and/or the editor(s). MDPI and/or the editor(s) disclaim responsibility for any injury to people or property resulting from any ideas, methods, instructions or products referred to in the content.